

## Electronic supplementary information for

### Nature-Inspired Salt Resistant Bimodal Porous Solar Evaporator for Efficient and Stable Water Desalination

Shuaiming He,<sup>1a</sup> Chaoji Chen,<sup>1a</sup> Yudi Kuang,<sup>1</sup> Ruiyu Mi,<sup>1</sup> Yang Liu,<sup>1</sup> Yong Pei,<sup>2</sup> Weiqing Kong,<sup>1</sup> Wentao Gan,<sup>1</sup> Hua Xie,<sup>1</sup> Emily Hitz,<sup>1</sup> Chao Jia,<sup>1</sup> Xi Chen,<sup>3</sup> Amy Gong,<sup>1</sup> Jianming Liao,<sup>4</sup> Jun Li,<sup>4</sup> Zhiyong Jason Ren,<sup>3</sup> Bao Yang,<sup>2</sup> Siddhartha Das,<sup>2</sup> Liangbing Hu<sup>1\*</sup>

1. Department of Materials Science and Engineering, University of Maryland, College Park, Maryland, 20742

2. Department of Mechanical Engineering, University of Maryland, College Park, Maryland, 20742

3. Department of Civil and Environmental Engineering and Andlinger Center for Energy and the Environment, Princeton University, Princeton, NJ, 08544

4. State Key Laboratory of Pulp and Paper Engineering, South China University of Technology, Guangzhou 510640, China

\* Email: [binghu@umd.edu](mailto:binghu@umd.edu)

<sup>a</sup> These authors contributed equally to this work.

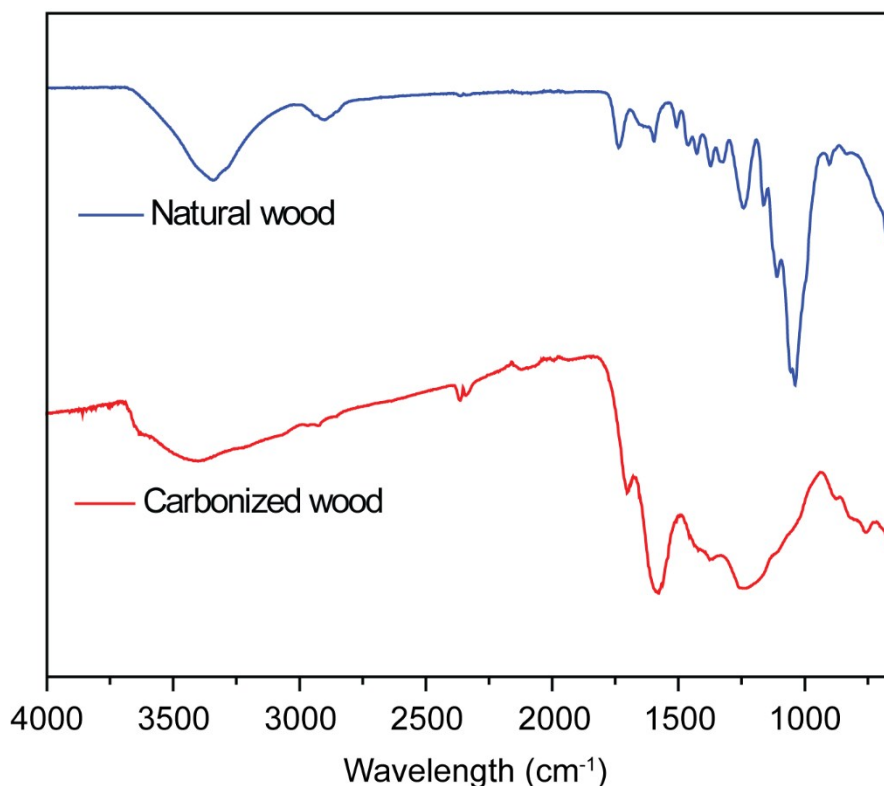


**Figure S1.** FT-IR spectra analyses of the bimodal evaporator (natural wood layer and the top surface carbonized layer). The newly presented wide peak between 3000 and 3700  $\text{cm}^{-1}$  of the surface carbonized layer shows that the amount of free hydroxyl group obviously decreases. And the newly emerged peak at around 1750  $\text{cm}^{-1}$  indicates that natural wood has been oxidized after carbonization.

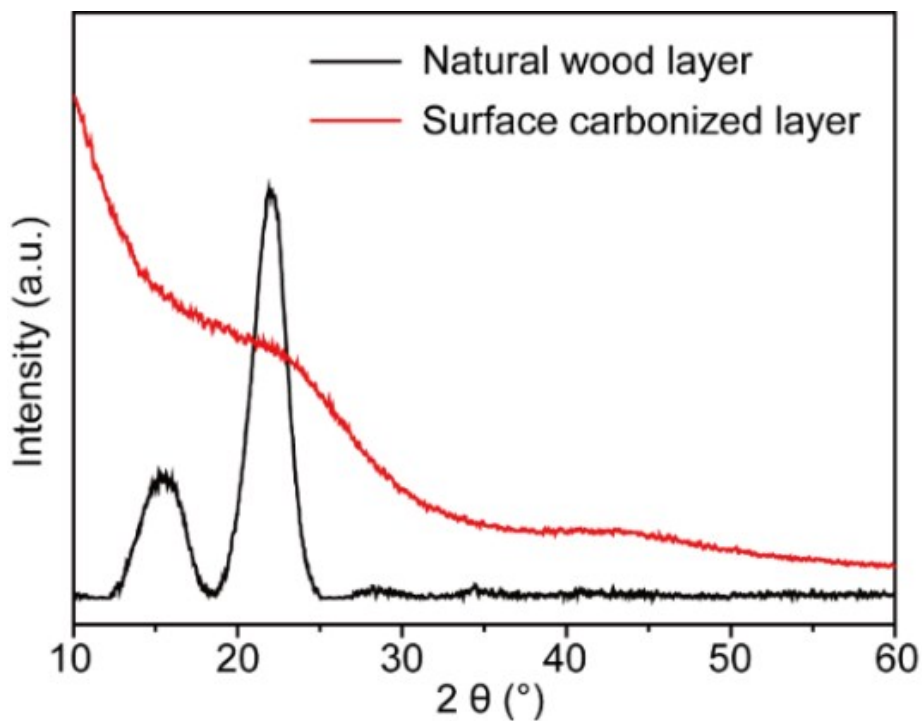


**Figure S2.** XRD patterns of the natural balsa wood and surface carbonized balsa wood layers.

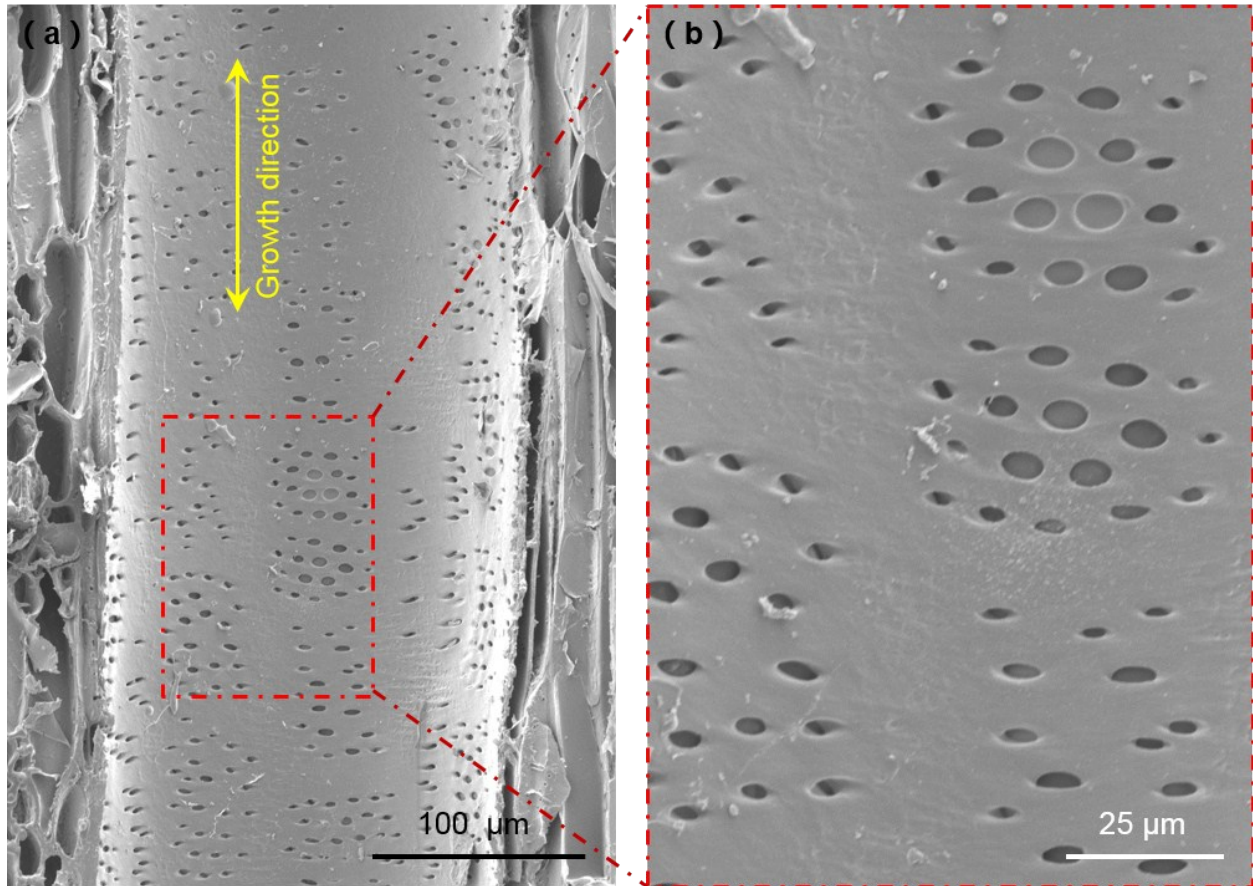


**Figure S3.** (a, b) SEM images shows numerous pits can be observed on the cell walls of the vessel channels, these pits make adjacent microchannels closely connected and are beneficial to transverse water transfer by diffusion and convection during solar desalination.

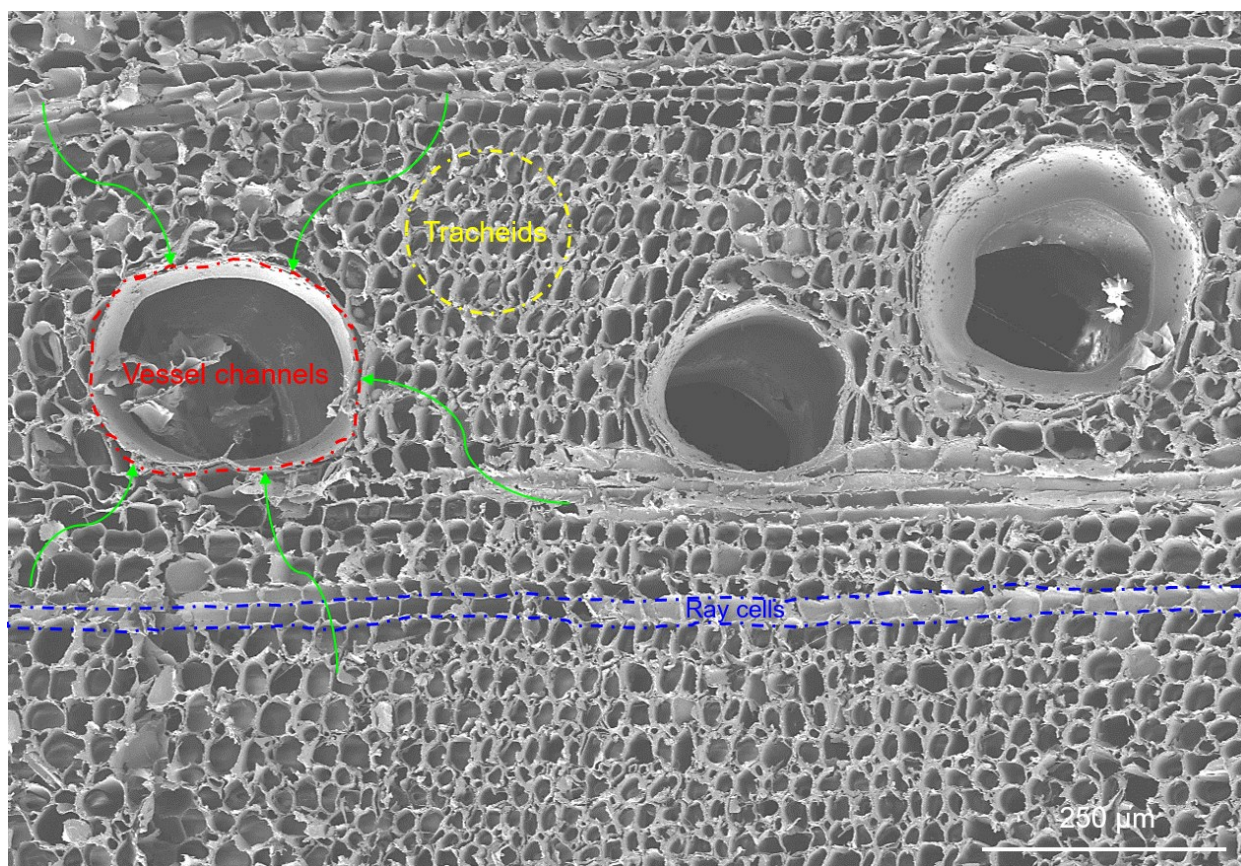


**Figure S4.** Top view SEM image of the bimodal evaporator. Note that the 3D interconnected mesoporous microstructures of natural balsa wood are well-preserved after carbonization. There exists efficient lateral brine diffusion and convection (through pits, ray parenchyma cells and nanopores) between the vessel channels and neighboring tracheids owing to the salt concentration differences during desalination (as shown by the red arrows).

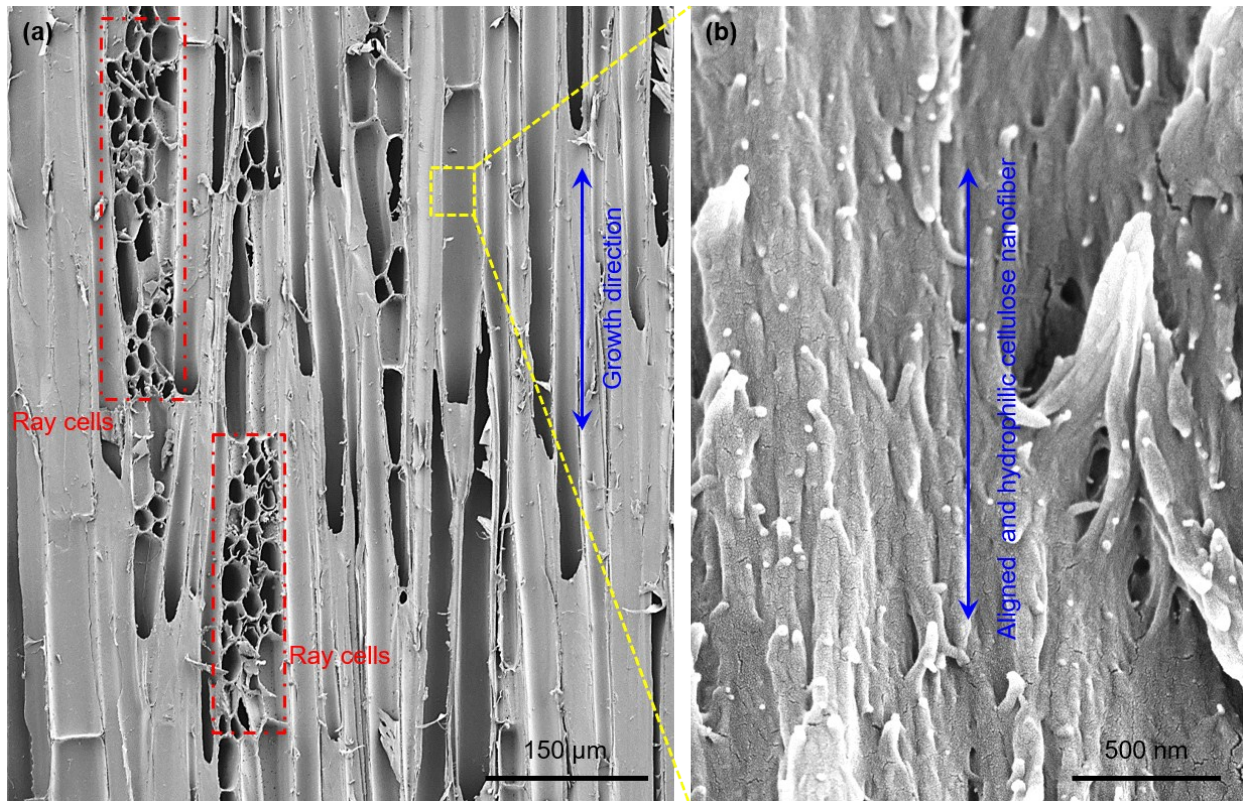


**Figure S5.** Cross-sectional SEM image of the bimodal evaporator. (a) The well-oriented long microchannels along the tree growth direction can help pump brine upward rapidly by capillary action. And the ray parenchyma cells (marked with red square dashed icon) can help transverse brine transport solar desalination. (b) High-magnification SEM image shows that numerous aligned hydrophilic cellulose microfibrils can help brine transport during solar desalination.

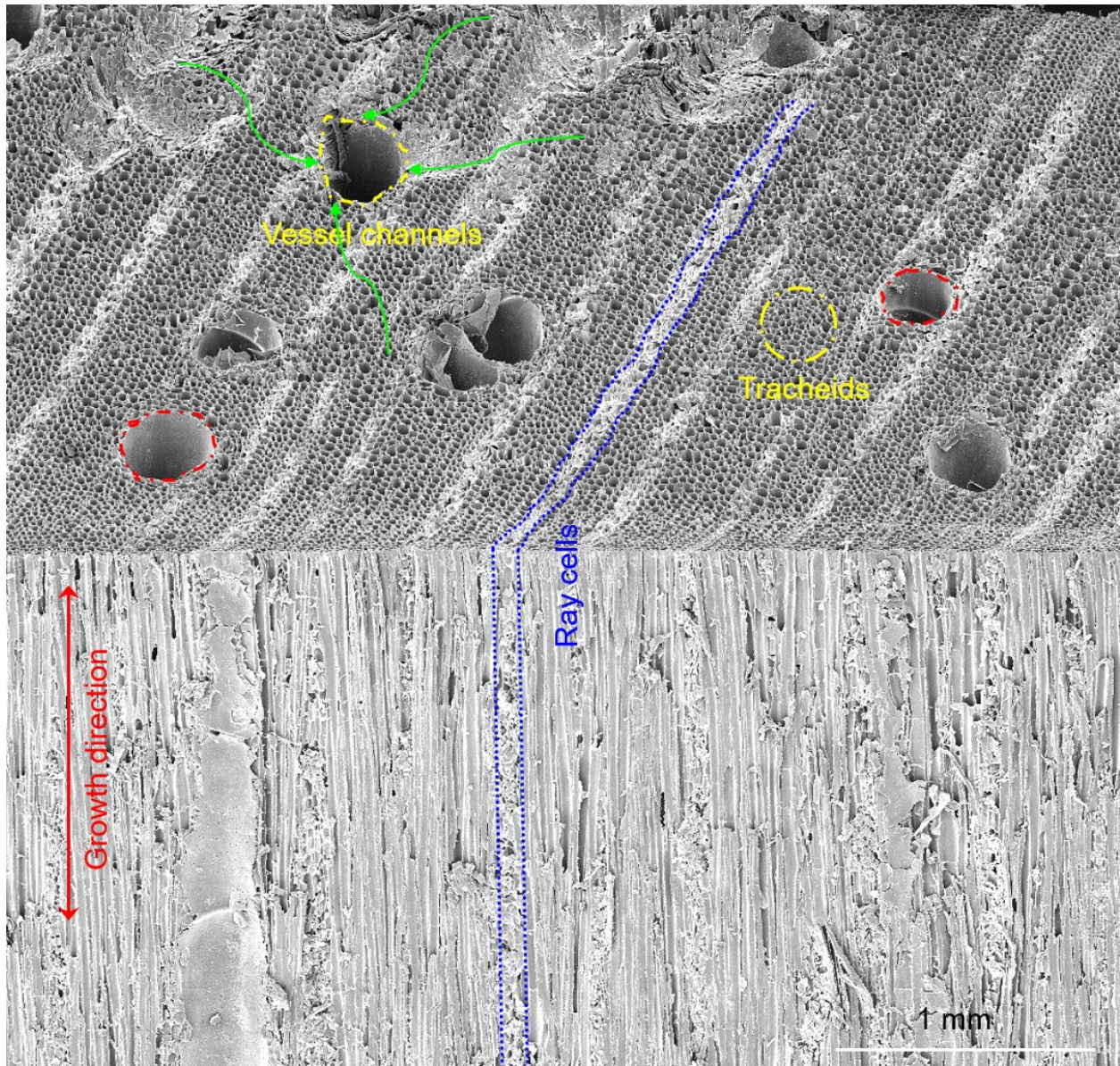


**Figure S6.** SEM image of long, aligned vessel channels and tracheids that are beneficial to rapid brine and steam transport during desalination operation. Sufficient brine can be transported to the surface of the wood evaporator through the wide vessel channels by capillary action to avoid salt accumulation. Simultaneously, the ray parenchyma cells that periodically penetrate the microchannels can help transverse brine transport during solar desalination. There exists efficient lateral brine diffusion and convection between the vessel channels and neighboring tracheids (as shown by the red arrows)

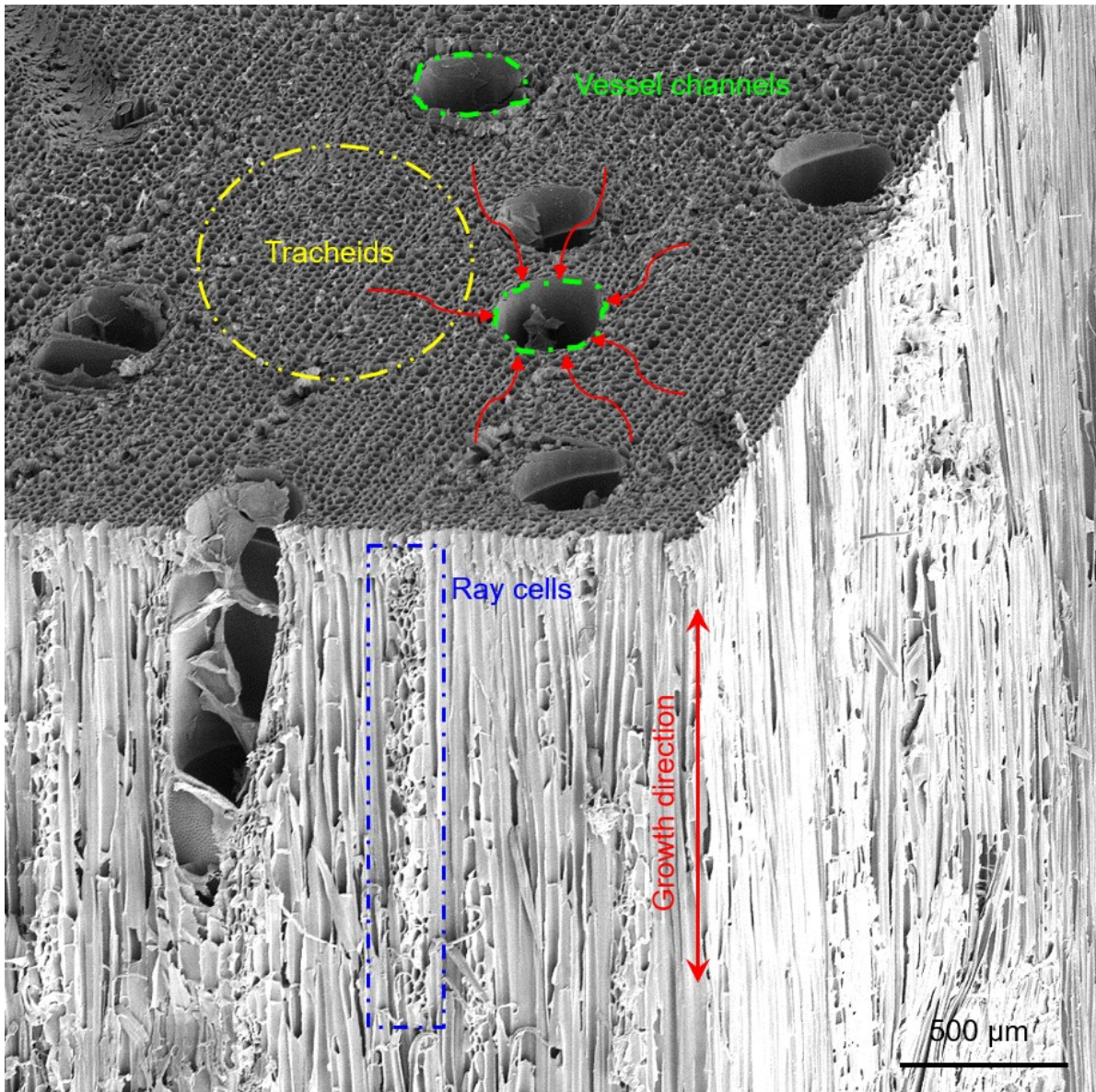


**Figure S7.** 3D SEM image shows that the numerous well-oriented bimodal microchannels can help transport brine upward by capillary action. Numerous ray cells that periodically penetrate the microchannels help transverse brine transport (by diffusion or convection) during solar desalination. These inherent microstructural characteristics can effectively avoid the salt accumulation on the top surface during long-term solar desalination.

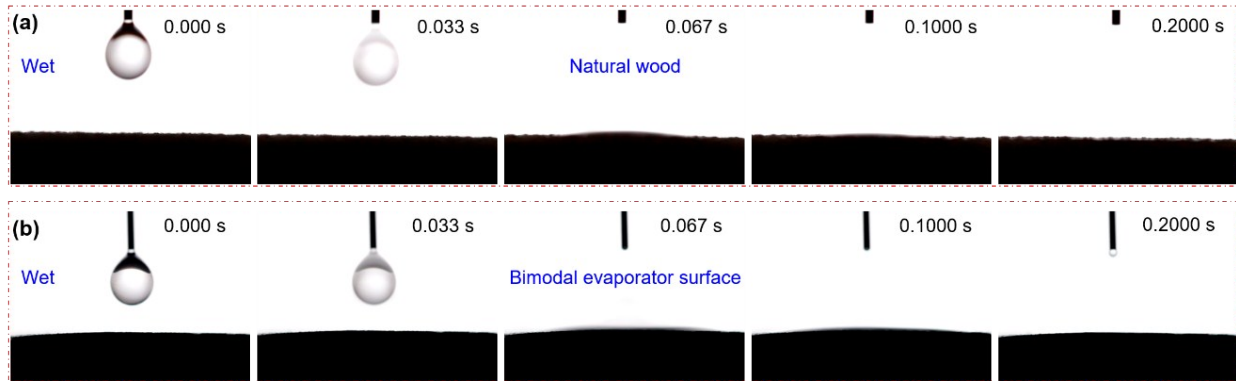


**Figure S8.** Time-lapse photography shows the hydrophilic properties of the natural wood and the bimodal evaporator under working (wet) conditions.

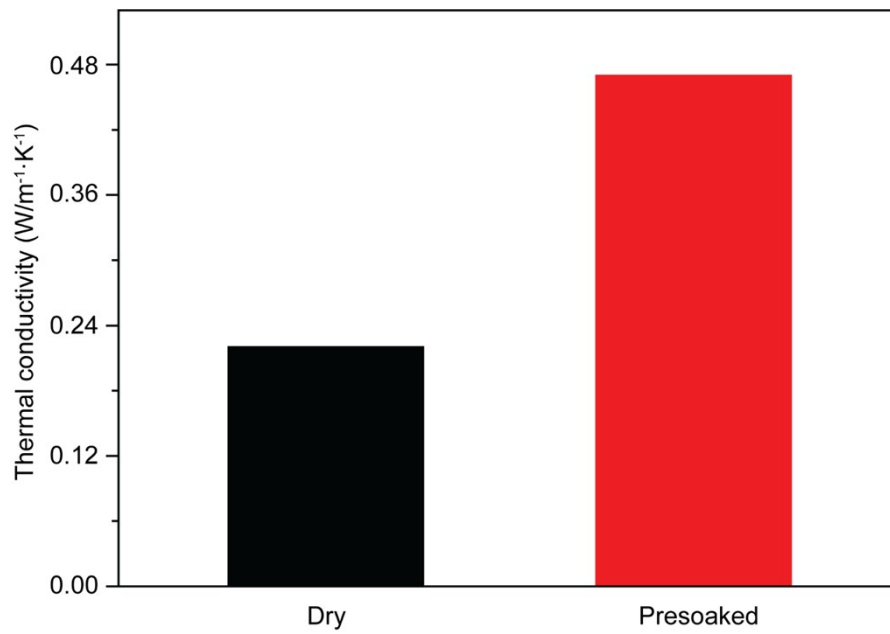


**Figure S9.** The thermal conductivities of the bimodal evaporator at dry and dynamic operating conditions.



**Figure S10.** The bimodal evaporator can float on brine or sea, which indicates this eco-friendly evaporator can help protect agricultural land and natural ecosystem from being utilized for energy-water nexus.

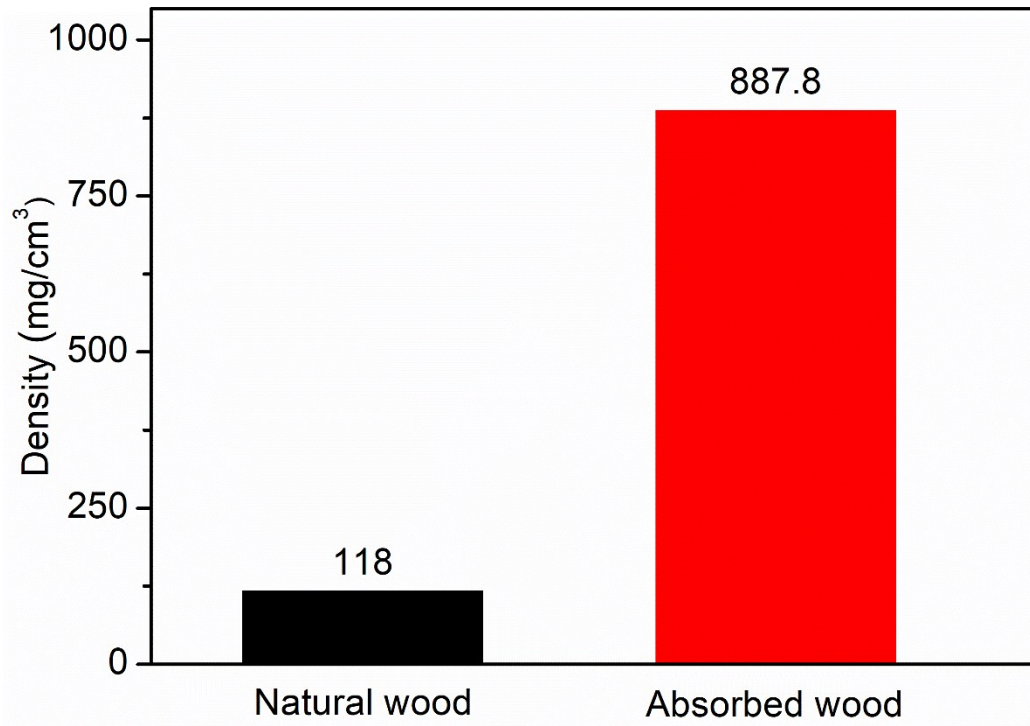


**Figure S11.** Density changes of the bimodal porous balsa wood before and after absorbing water under 6 suns irradiation for 7 h.

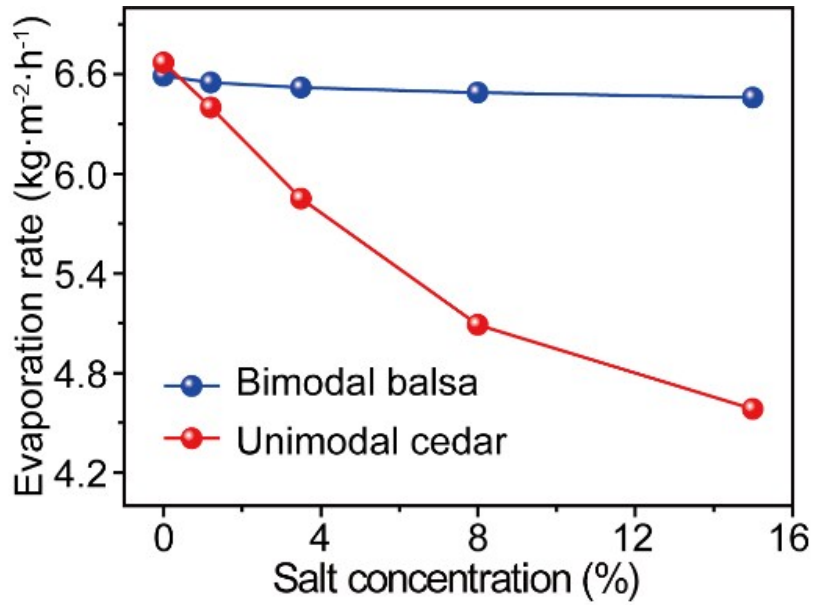


**Figure S12.** The effect of salt concentration on the evaporation rates of the bimodal balsa and unimodal cedar samples under 6 suns.

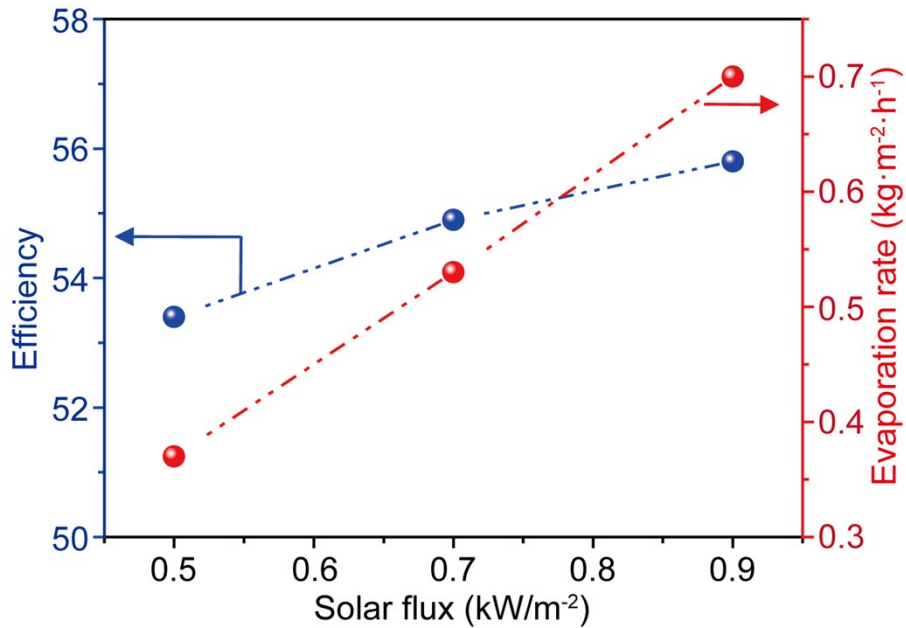


**Figure S13.** The evaporation rate and energy-conversion efficiency of the bimodal evaporator under low light intensity (< 1 kW/m<sup>2</sup>).

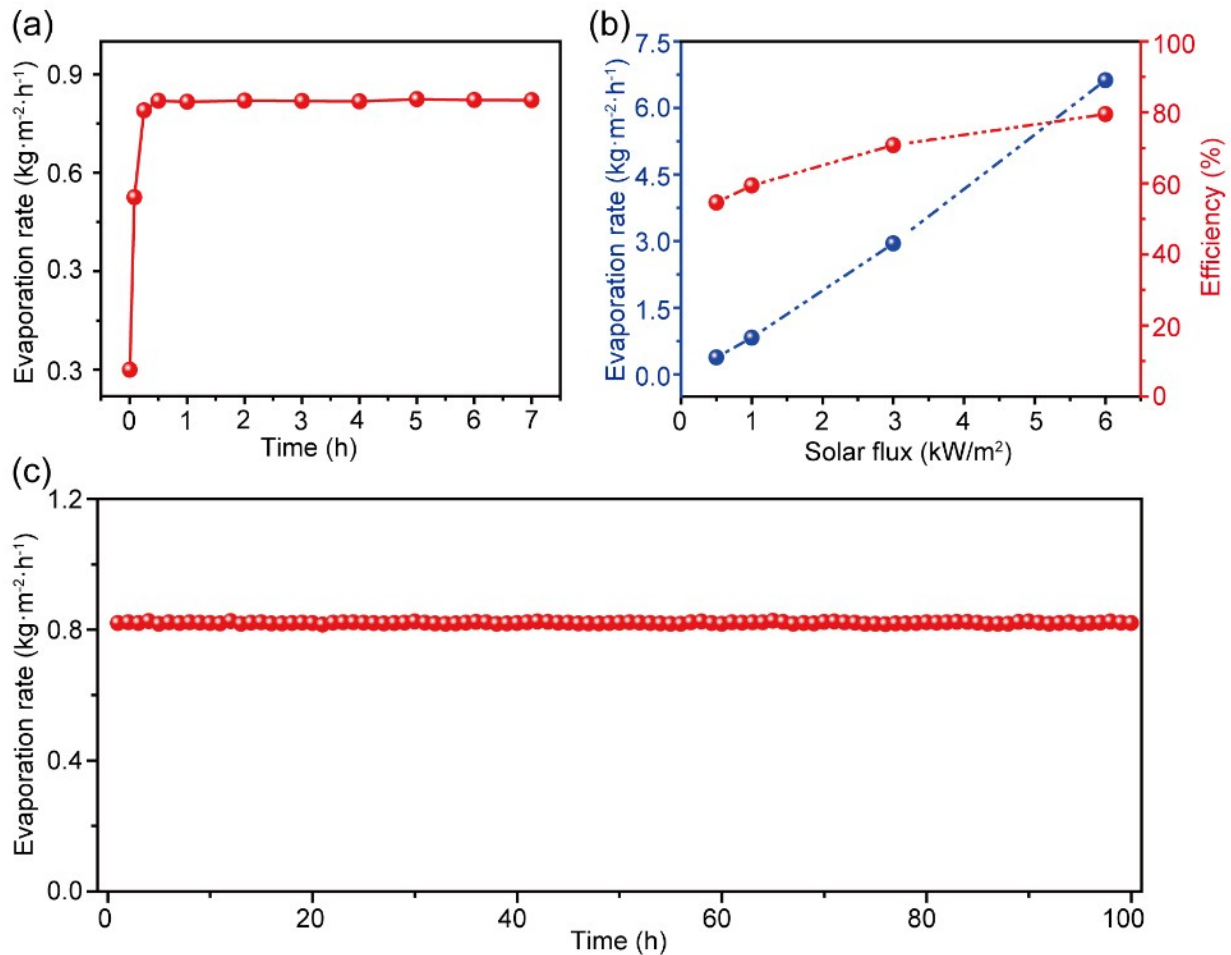


**Figure S14.** (a) Time-dependent evaporation rate of our bimodal evaporator in treating actual seawater samples under 1 sun illumination. (b) The evaporation rates and energy-conversion efficiencies of the bimodal evaporator as a function of solar flux. (c) The long-term stability test of our bimodal evaporator.

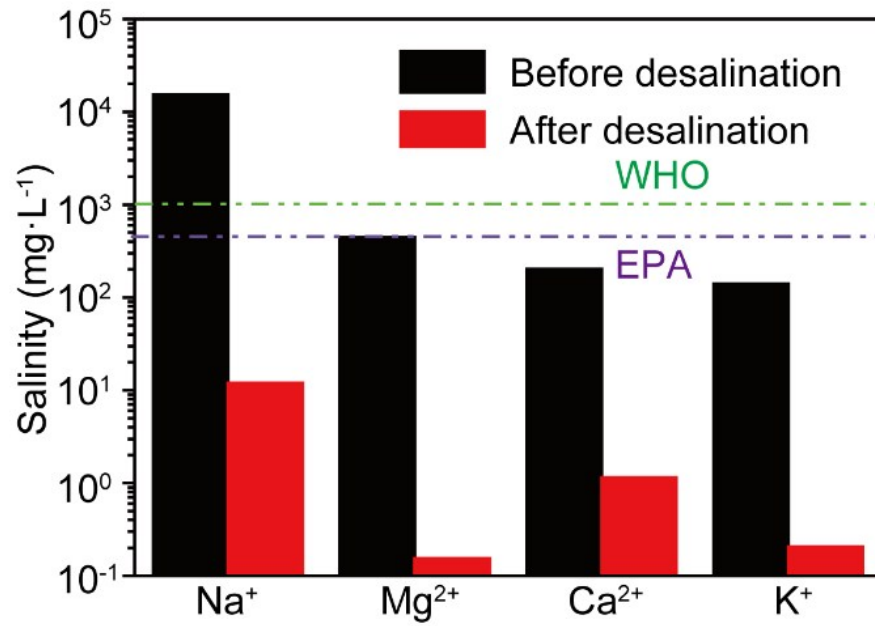


**Figure S15.** Salinity changes of the seawater before and after desalination.

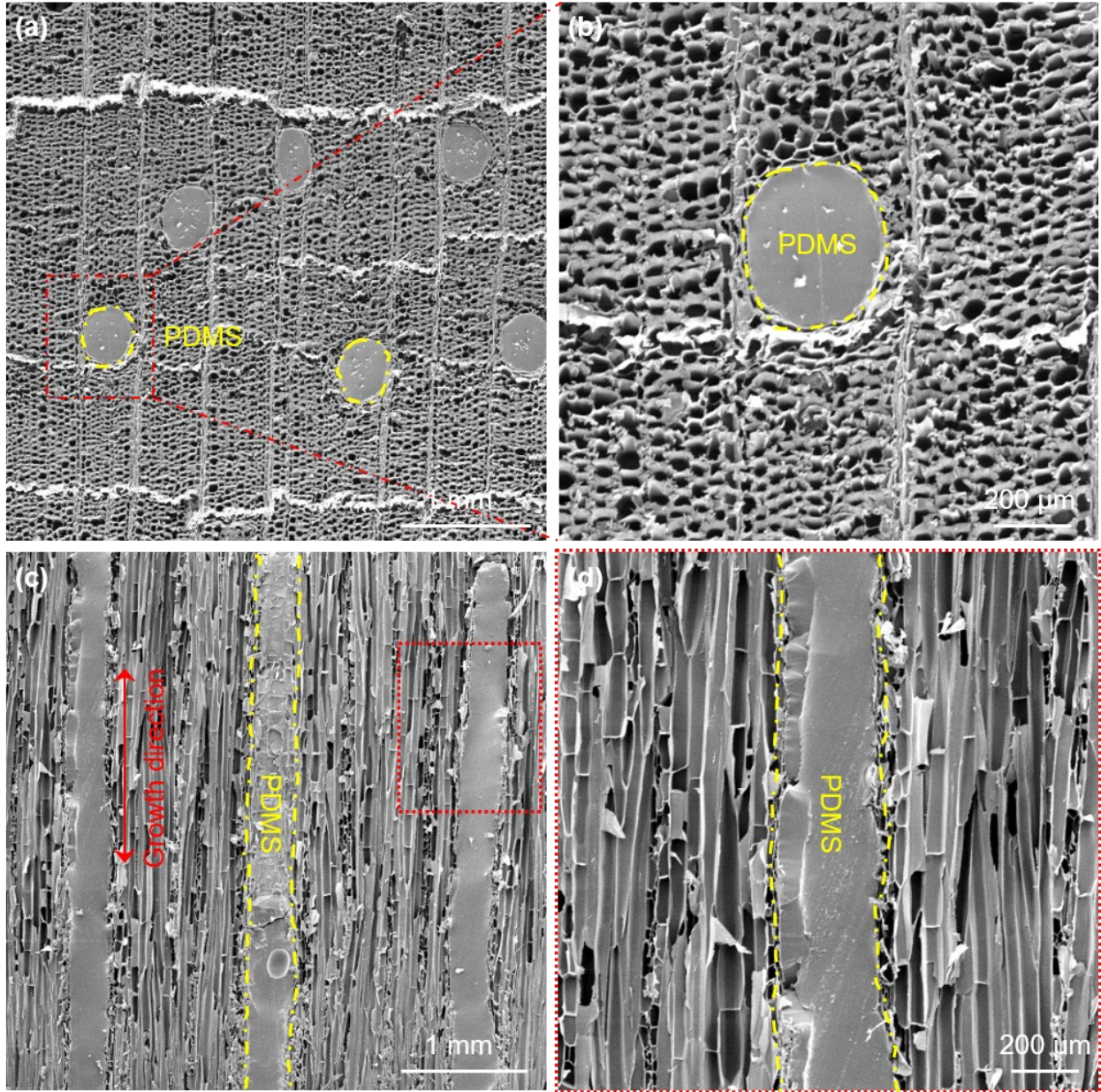


**Figure S16.** Top view (a, b) and side view (c, d) SEM images of the control sample PDMS/balsa evaporator. It can be observed that the wide vessel channels are blocked by PDMS while small size tracheids are wide open for brine transport during desalination operation. The infiltrated PDMS reduces the speed of brine transport upward and impedes the diffusion and convection of brine between the microchannels, thus severe salt accumulation can be observed on the surface of the control sample.

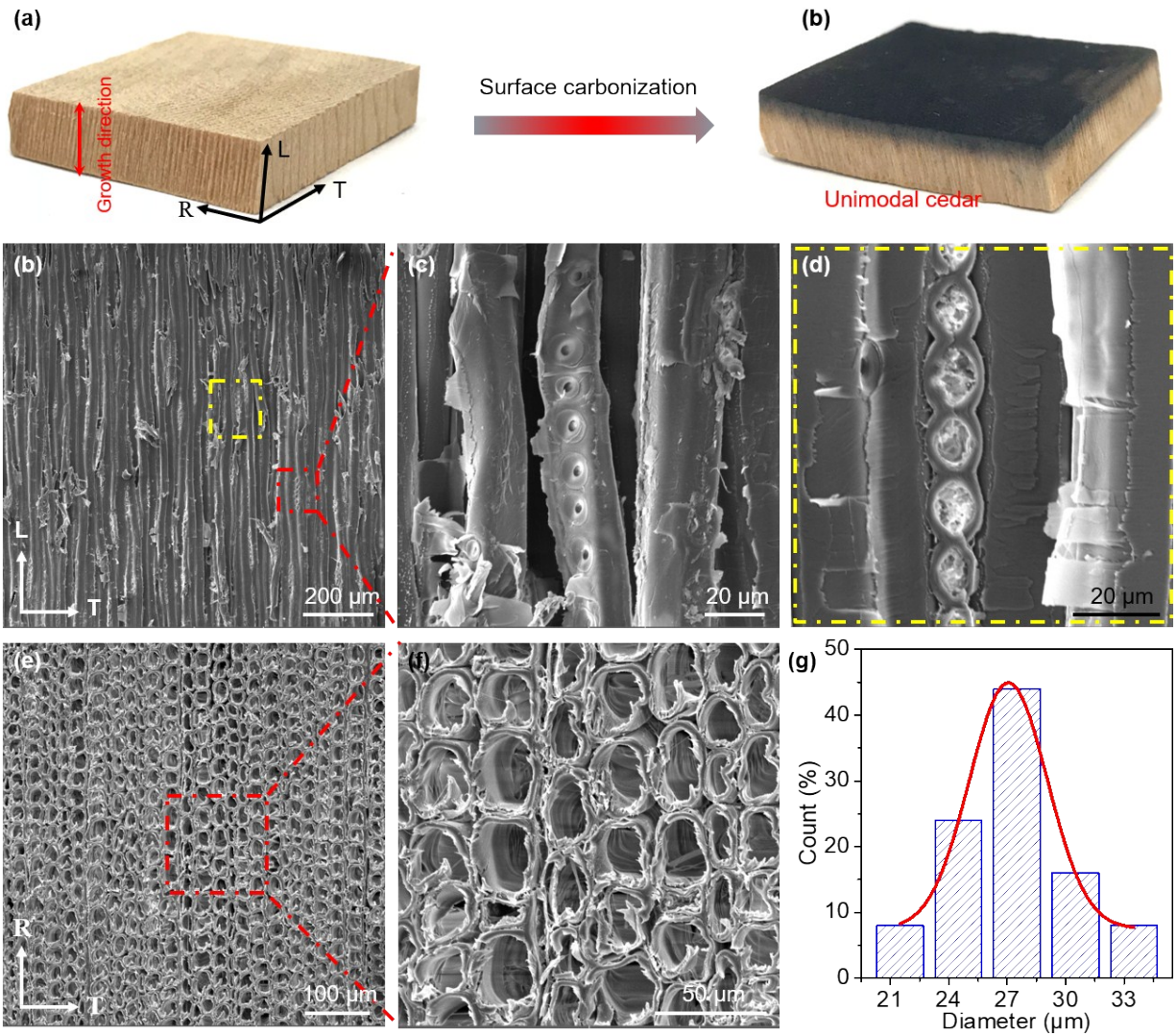


**Figure S17.** Microstructural characterizations of another control sample: the unimodal evaporator (cedar). (a, b) Digital images of natural cedar and the unimodal evaporator. (c) Side view SEM image shows that numerous pits can be observed in the unimodal evaporator. (d) Magnified image of c shows numerous ray cells can be observed on the cell walls of microchannels, these pits and ray cells can act as paths for lateral water transport. (e) Top view SEM image shows the unimodal evaporator has comparatively uniform pore size distribution. (f) Magnified SEM image of e shows the uniform pore size distribution. (g) Pore size distribution statistics of the microchannels.

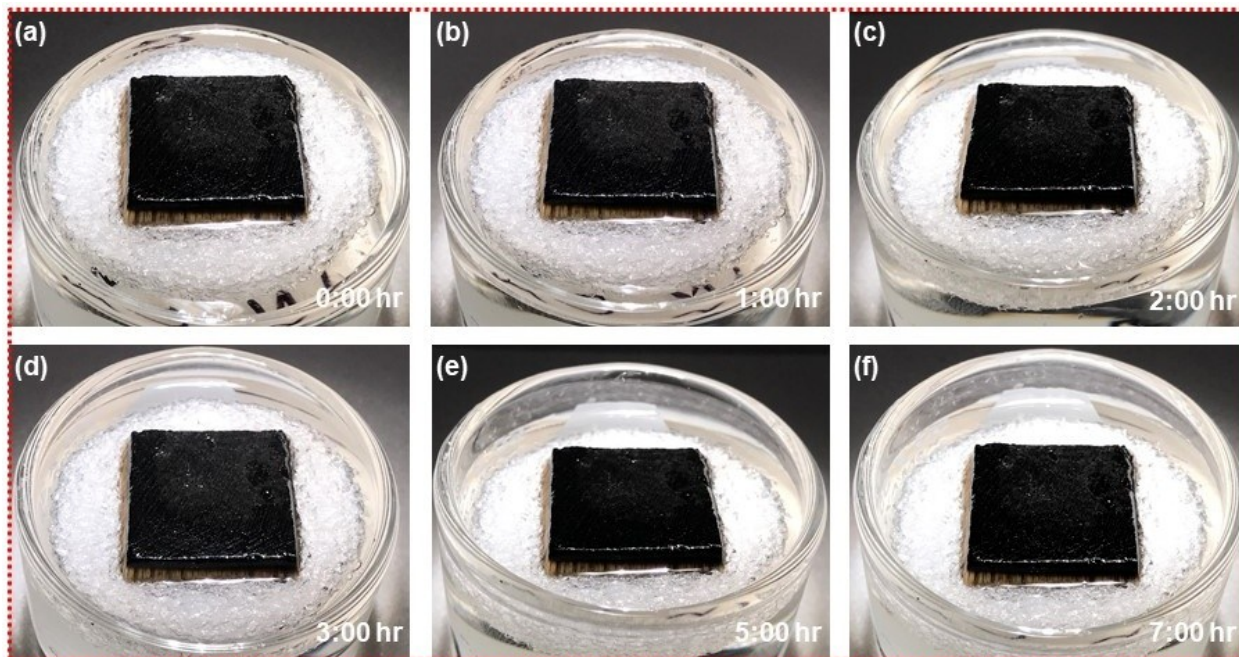


**Figure S18.** Digital images of the bimodal evaporator over 7 h under 6 suns illumination intensities. We did not observe any salt accumulation on the surface. This indicates the excellent salt resistant property of the evaporator. The white foam can help prevent the incident light from being directly absorbed by the surrounding brine.

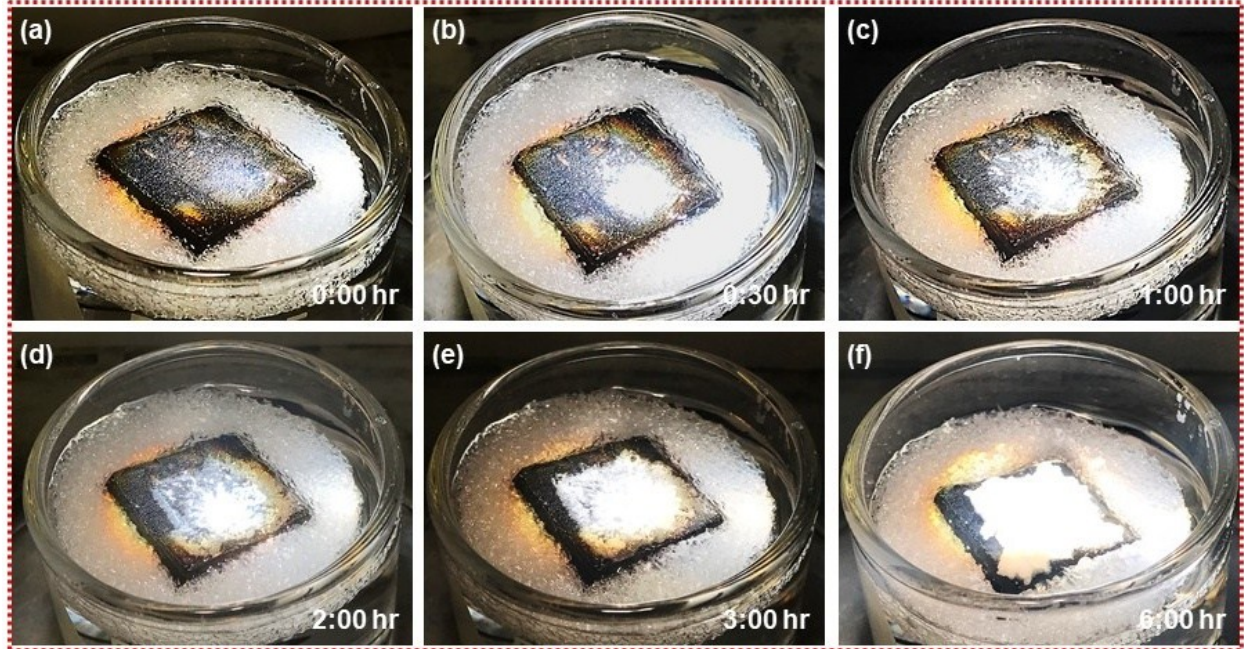


**Figure S19.** Time elapsed snapshots of the control sample PDMS/balsa evaporator. Severe salt accumulation can be observed after 7 h of 6 suns illumination, these salts severely inhibits the adsorption of incident sunlight thus inevitably results in the performance deterioration of the device. Thus, analyses results indicate that the wide vessel channels in the bimodal evaporator play an important role in avoiding salt accumulation because they can supply sufficient brine transport by capillary action.

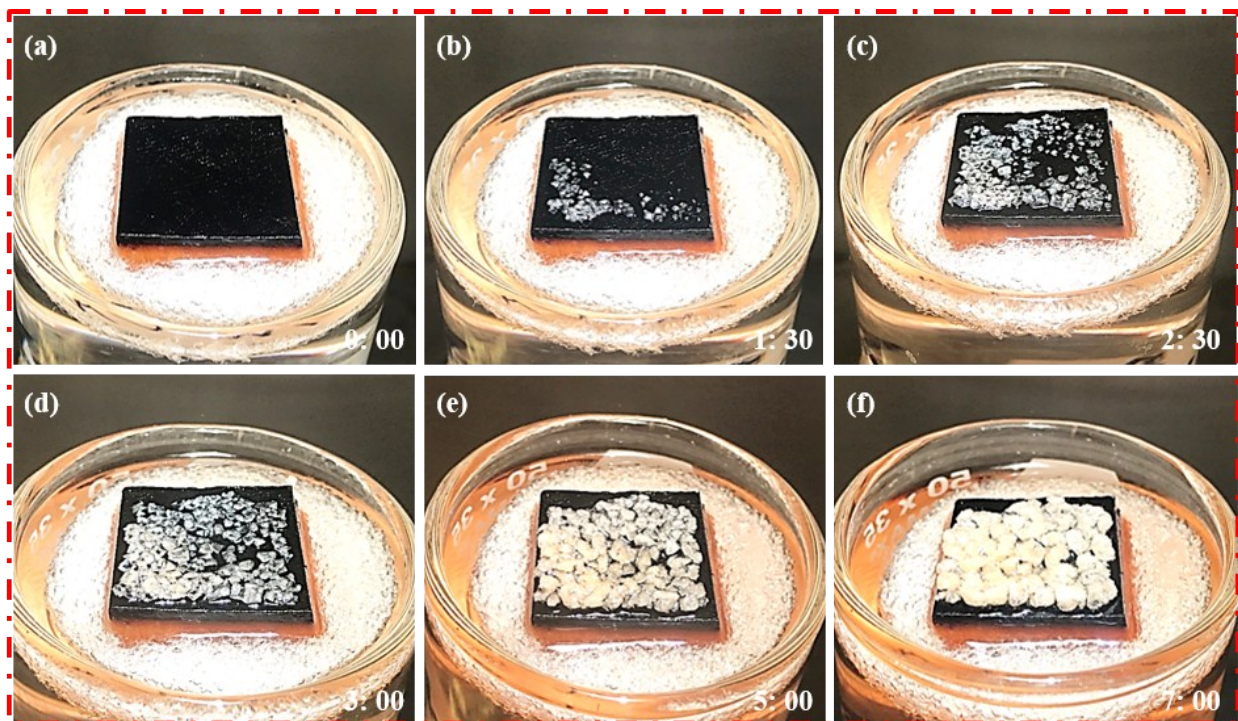


**Figure S20.** Time elapsed snapshots of the second control sample unimodal cedar evaporator. Severe salt accumulation can also be observed after 7 h of 6 suns illumination, these salts severely deteriorated of the performance of the device. Sufficient brine transport upward to the top surface cannot be guaranteed in the unimodal evaporator due to the lack of wide microchannels.

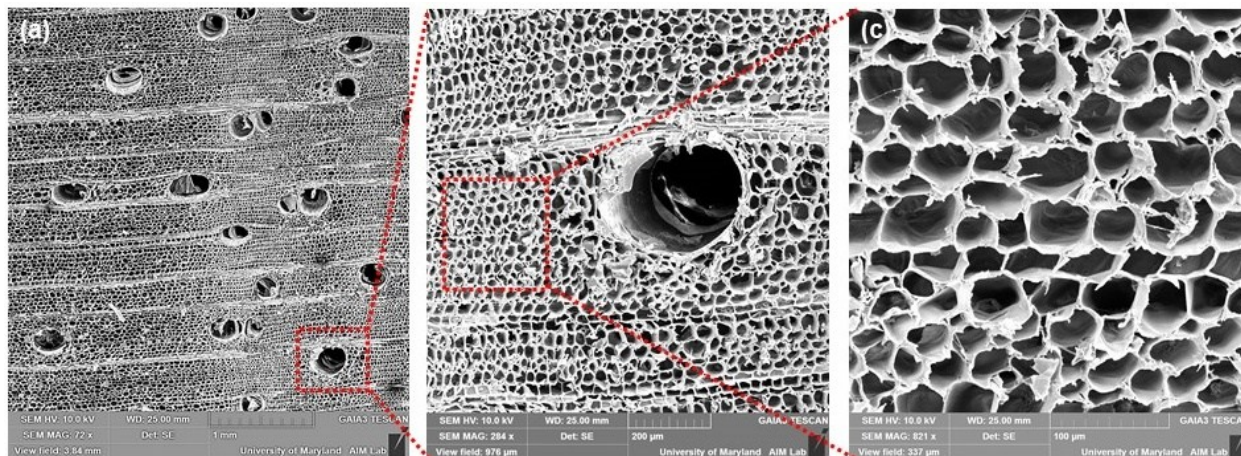


**Figure S21.** Top view SEM images of the bimodal evaporator after long-term cycling (20 days, 7 h per day). We did not observe any salt crystals within the microchannels.

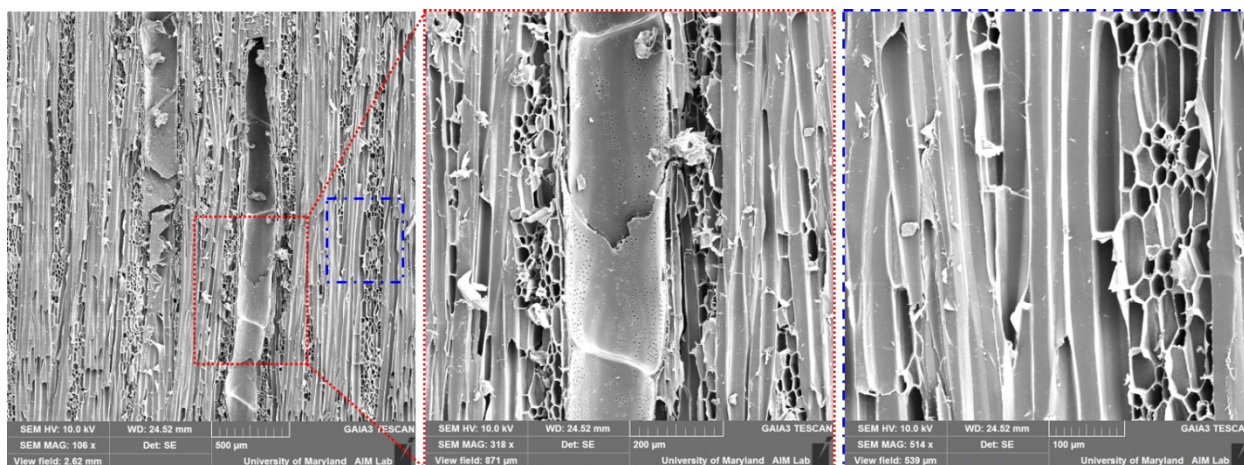


**Figure S22.** Side view SEM images of the bimodal evaporator after long-term cycling (20 days, 7 h per day). We did not observe any salt crystals within the microchannels.

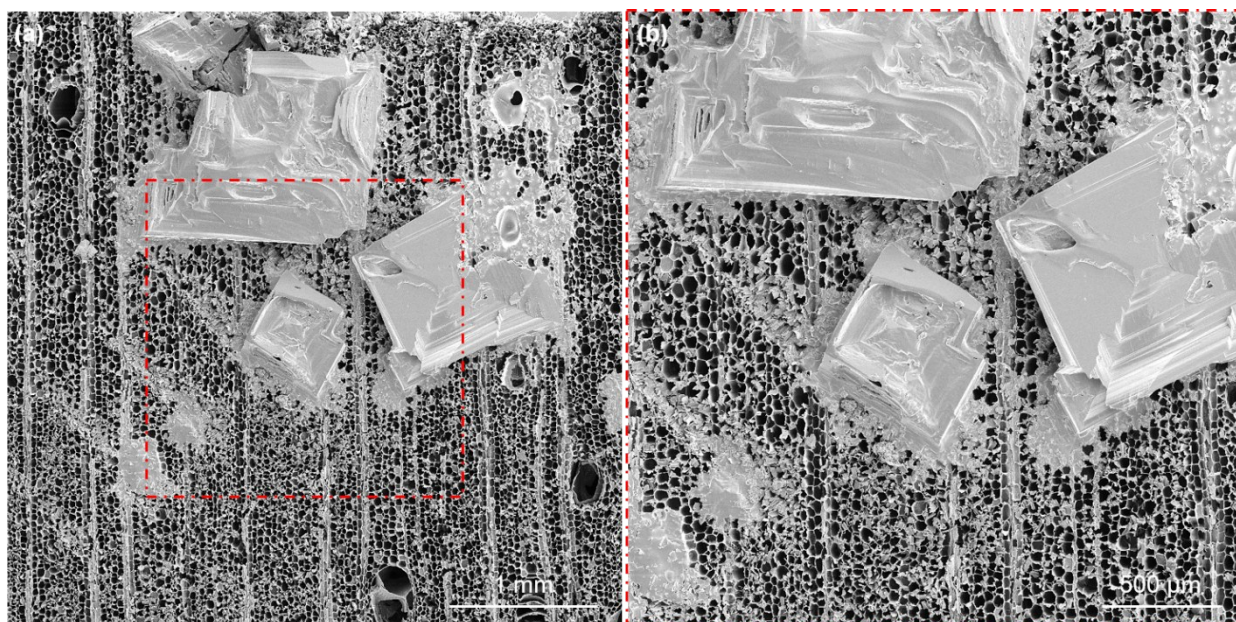


**Figure S23.** SEM images of the PDMS/balsa (control sample) after 45 min of 6 suns illumination, salt crystals begin to accumulate on the surface, these accumulated salts could severely affect the performance of the device.

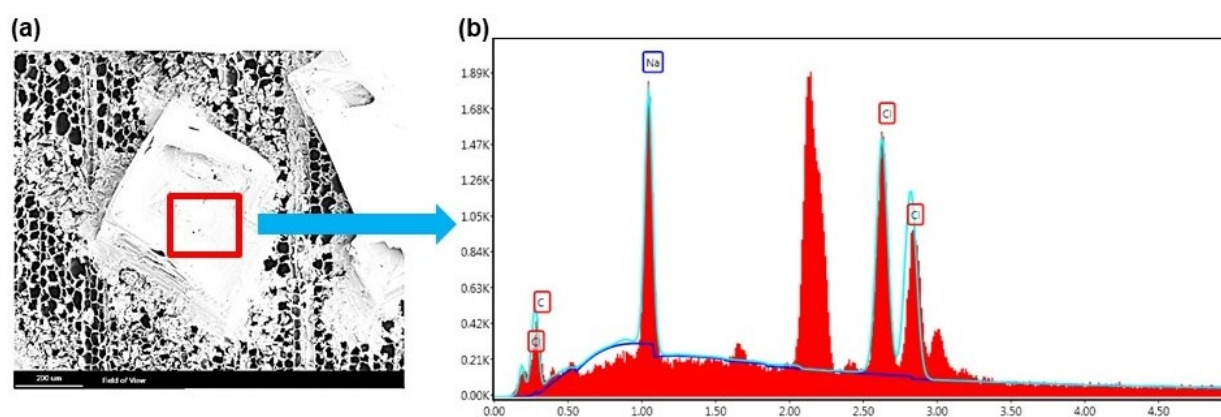


**Figure S24.** SEM-EDS of the PDMS/balsa after 45 min of 6 suns illumination confirms that the crystals are NaCl.

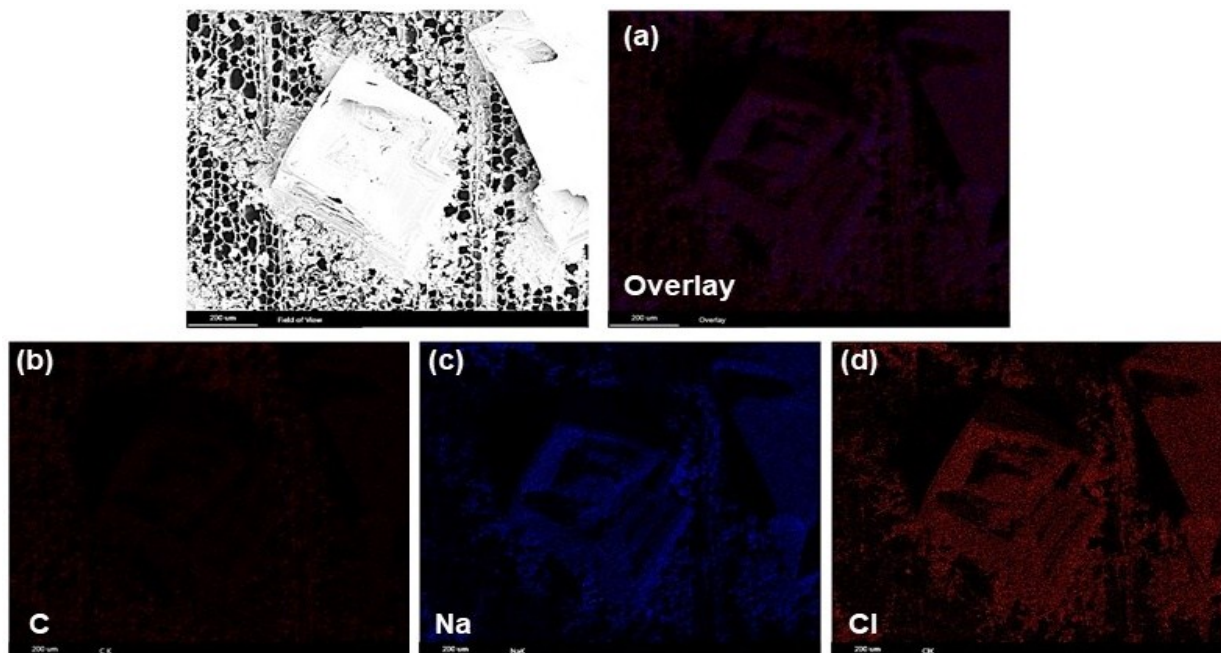


**Figure S25.** SEM-EDS mapping of the control sample PDMS/balsa after 45 min of 6 suns illumination further confirms that the crystals are NaCl.

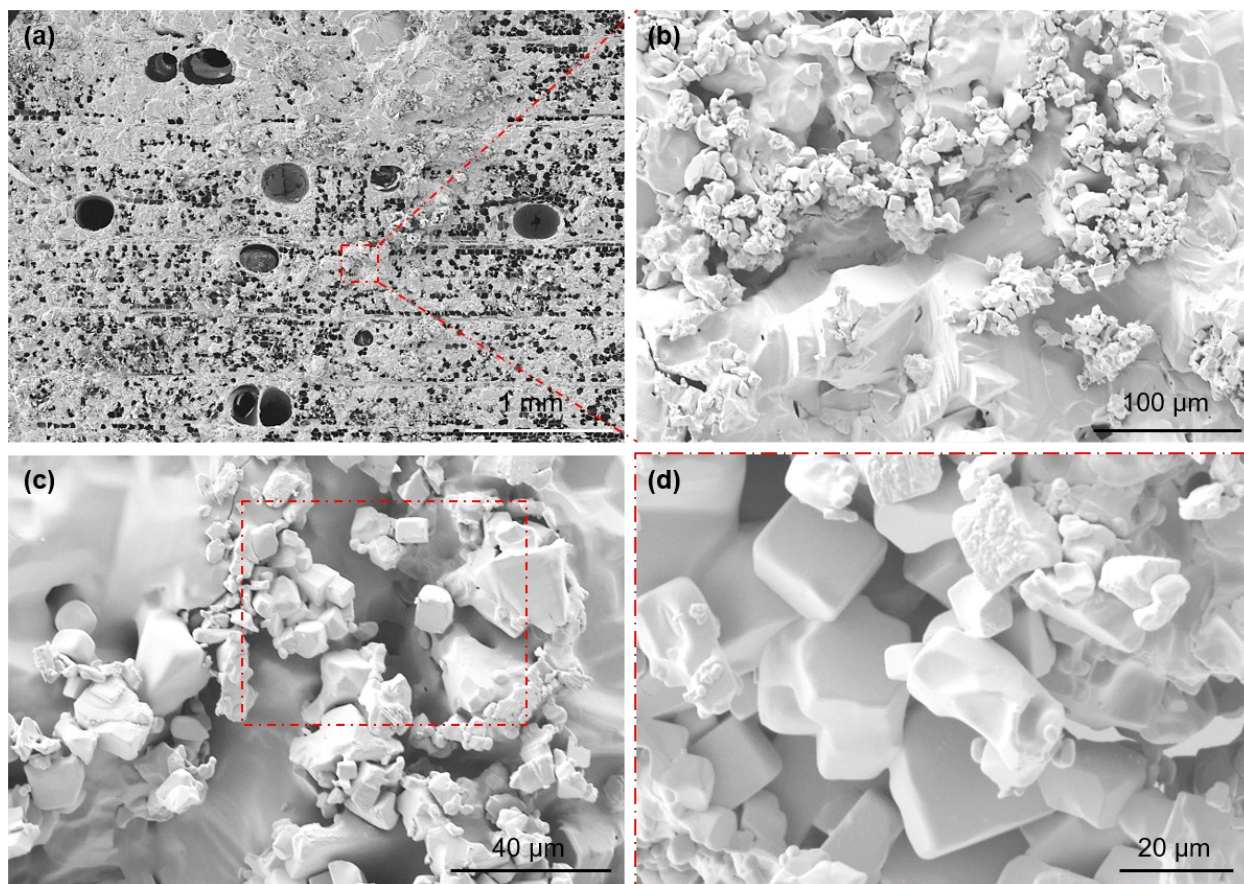


**Figure S26.** SEM images of the PDMS/balsa after 2h of 6 suns illumination, a lot of salt crystals deposit on the wood surface and severely block these microchannels and reduce the evaporation efficiency.

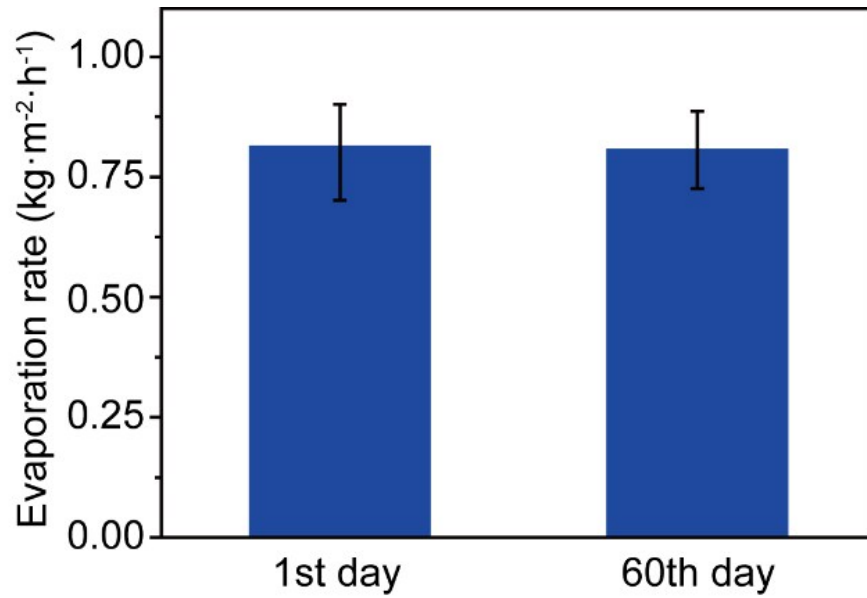


**Figure S27.** The stability test of our evaporator after immersion in seawater for 60 days.

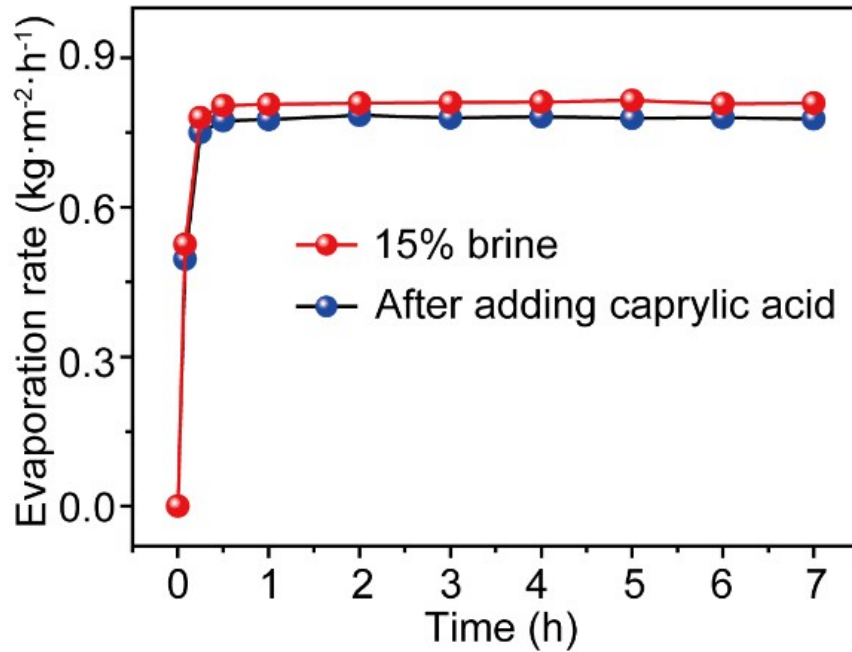


**Figure S28.** The effect of caprylic acid on the performance of our bimodal evaporator.

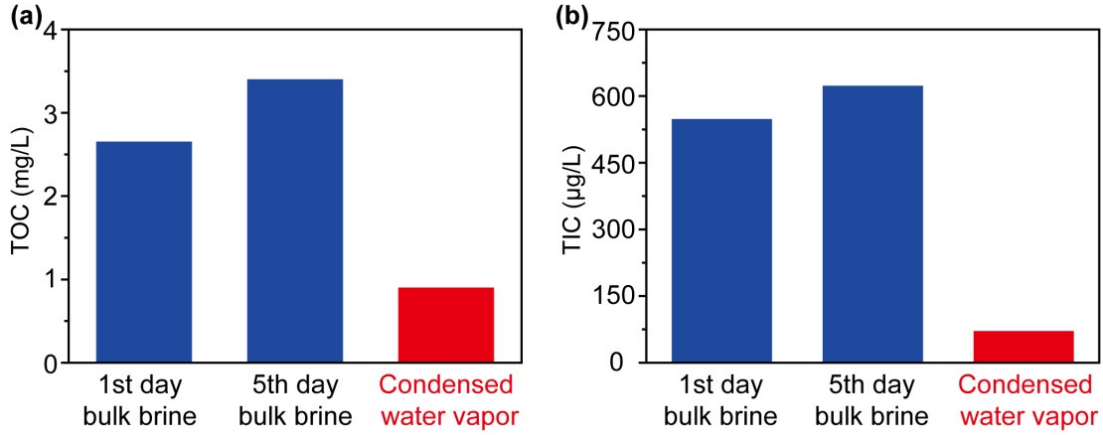


**Figure S29.** The (a) TOC and (b) TIC contents in the bulk brine solution beneath the evaporator after the evaporator ran for 1 and 5 days (7 hours per day, 1 sun). The red columns in (a) and (b) represent the TOC and TIC contents in the collected condensed water vapor, respectively.

### **Scaling Calculations:**

The principle of operation of this bimodal evaporator requires the prevention of salt accumulation at the top surface of the wood. This is possible if the rate of diffusion of the accumulated salt through the ray cells and pits is larger than the rate of the evaporation-induced salt accumulation at the top surface of the wood.

Let us consider that the rate of evaporation (in  $kg / (m^2 h)$ ) is  $e_{evap}$ . If the salt concentration of the brine solution is  $x$  g/cc or  $10^3 x$  kg/m<sup>3</sup>, and the density of the brine solution is  $\rho$  kg/m<sup>3</sup>, then this evaporation rate will imply a per unit area salt accumulation rate of

$$a_{salt, acc} = \left( \frac{10^3 x}{\rho - 10^3 x} e_{evap} \right) \frac{kg}{m^2 h} = \left( \frac{1}{3600} \frac{10^3 x}{\rho - 10^3 x} e_{evap} \right) \frac{kg}{m^2 s}. \quad (1)$$

In order to ensure that there is no accumulation of salt, the rate of diffusive transport  $a_{salt, Diff}$  of the accumulated salt through the ray cells and pits should be larger than  $a_{salt, acc}$ . We can express  $a_{salt, Diff}$  as:

$a_{salt, Diff}$  as:

$$a_{salt,Diff} \sim D \frac{dc}{dx} \sim D \frac{c_0}{l}. \quad (2)$$

Here  $c_0 \sim 10^3 x \text{ kg/m}^3$  is the salt concentration of the brine,  $D = 1.6 \times 10^{-9} \text{ m}^2/\text{s}$  is the diffusivity of the salt in water (See J. Appl. Polym. Sci. 2007, 106, 2536-2542.), and 700 microns = 0.0007 m, is the length scale over which the diffusion occurs. Accordingly, we can write (using  $x = 0.035$ ,  $\rho = 1030$ , and  $e_{evap} = 6.4$ ):

$$\frac{a_{salt,Diff}}{a_{salt,acc}} \sim \frac{D \frac{c_0}{l}}{\frac{1}{3600} \frac{10^3 x}{\rho - 10^3 x} e_{evap}} \sim \frac{D \frac{10^3 x}{l}}{\frac{1}{3600} \frac{10^3 x}{\rho - 10^3 x} e_{evap}} \sim \frac{3600 D (\rho - 10^3 x)}{l e_{evap}} \quad (3)$$

$$\sim \frac{3600 \times 1.6 \times 10^{-9} \times (1030 - 10^3 \times 0.035)}{(7 \times 10^{-4}) (6.4)} \sim 1.29.$$

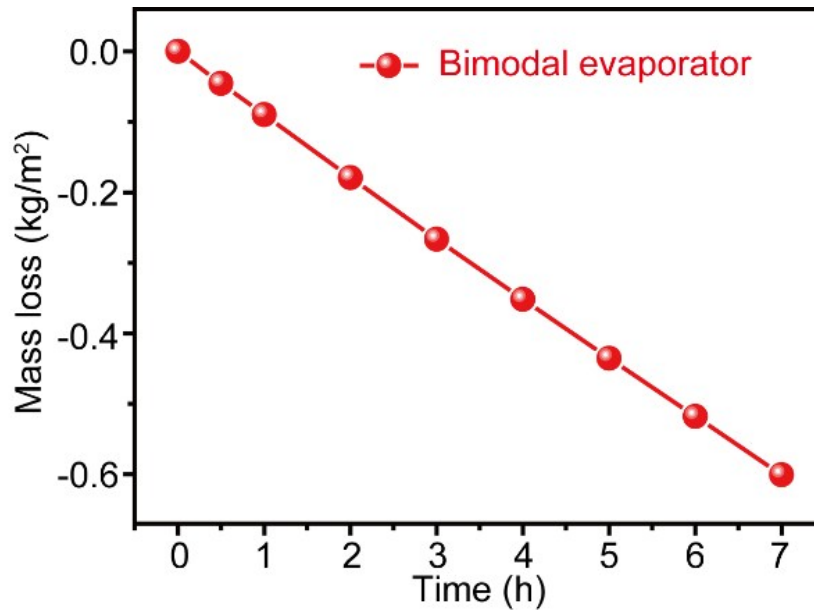


**Figure S30.** Evaporation rates of the bimodal evaporator under dark fields.

**Table S1.** Comparison of the efficiency, price, and performance of various steam-generation devices.

Material	Efficiency	Price	Salt concentration studied (wt%)	Continuous testing time	Ref.
<b>Bimodal evaporator</b>	<b>57.2% under 1 sun</b>	<b>low</b>	<b>15%</b>	<b>7 h, 20 cycle</b>	<b>This work</b>
	<b>59.4% under 1 sun</b>	<b>low</b>	<b>1.1 %</b>	<b>100 h</b>	
Nanoporous anodic aluminium oxide membrane (AAM) close packed aluminium NPs.	57% under 1 sun	medium	2.75%	1 h	1
Nanosized titanium sesquioxide (Ti <sub>2</sub> O <sub>3</sub> ) /cellulose membrane (CM)	<65% under 1 sun <75% under 5 sun	high	0%	1 h	2
GO/polystyrene foam	80% under 1 sun	high	1.4%	0.83 h	3
Nylon/carbon cloth	~83% under 1 sun	medium	3.5%	2 h	4
Janus Absorbers	~51% under 1 sun	high	3.5%	0.75 h	5
2D SCS disks	~ 55% under 1 sun	high	15%	1 h	6
Graphene Oxide Leaf	~85% under 1 sun	high	3.5%	2 h	7
Wick/polystyrene	~55% under 1 sun	medium	3%	3h, 0.7-1 sun	8
Au absorbers (200 nm)	49% under 1 sun	high	0	1 h	9
GO/SBA-15	~77% under 1 sun	high	3.5%	3h	10
Au/NPT plasmonic absorbers	~63%	high	0	1h	11
3D graphene	87%	high	0.9%	4h, 0.5-0.6 sun	12

References:

- [1] Zhou, Lin, Yingling Tan, Jingyang Wang, Weichao Xu, Ye Yuan, Wenshan Cai, Shining Zhu, and Jia Zhu. "3D self-assembly of aluminium nanoparticles for plasmon-enhanced solar desalination." *Nature Photonics* 10, no. 6 (2016): 393.
- [2] Wang, Juan, Yangyang Li, Lin Deng, Nini Wei, Yakui Weng, Shuai Dong, Dianpeng Qi, Jun Qiu, Xiaodong Chen, and Tom Wu. "High-Performance Photothermal Conversion of Narrow-Bandgap Ti<sub>2</sub>O<sub>3</sub> Nanoparticles." *Advanced Materials* 29, no. 3 (2017): 1603730.
- [3] Li, Xiuqiang, Weichao Xu, Mingyao Tang, Lin Zhou, Bin Zhu, Shining Zhu, and Jia Zhu. "Graphene oxide-based efficient and scalable solar desalination under one sun with a confined 2D water path." *Proceedings of the National Academy of Sciences* 113, no. 49 (2016): 13953-13958.

- [4] Jin, Yong, Jian Chang, Yusuf Shi, Le Shi, Seunghyun Hong, and Peng Wang. "A highly flexible and washable nonwoven photothermal cloth for efficient and practical solar steam generation." *Journal of Materials Chemistry A* 6, no. 17 (2018): 7942-7949.
- [5] Xu, Weichao, Xiaozhen Hu, Shendong Zhuang, Yuxi Wang, Xiuqiang Li, Lin Zhou, Shining Zhu, and Jia Zhu. "Flexible and salt resistant Janus absorbers by electrospinning for stable and efficient solar desalination." *Advanced Energy Materials* 8, no. 14 (2018): 1702884.
- [6] Shi, Yusuf, Chenlin Zhang, Renyuan Li, SifeiZhuo, Yong Jin, Le Shi, Seunghyun Hong, Jian Chang, Chisiang Ong, and Peng Wang. "Solar Evaporator with Controlled Salt Precipitation for Zero Liquid Discharge Desalination." *Environmental Science &Technology* 52, no. 20 (2018): 11822-11830.
- [7] Finnerty, Casey, Lei Zhang, David L. Sedlak, Kara L. Nelson, and Baoxia Mi. "Synthetic graphene oxide leaf for solar desalination with zero liquid discharge." *Environmental science & technology* 51, no. 20 (2017): 11701-11709.
- [8] Ni, George, SeyedHadiZandavi, SeyyedMorteza Javid, Svetlana V. Boriskina, Thomas A. Cooper, and Gang Chen. "A salt-rejecting floating solar still for low-cost desalination." *Energy & Environmental Science* 11, no. 6 (2018): 1510-1519.
- [9] Zhou, Lin, Shendong Zhuang, Chengyu He, Yingling Tan, Zhenlin Wang, and Jia Zhu. "Self-assembled spectrum selective plasmonic absorbers with tunable bandwidth for solar energy conversion." *Nano Energy* 32 (2017): 195-200.
- [10] Shi, Le, Yuchao Wang, Lianbin Zhang, and Peng Wang. "Rational design of a bi-layered reduced graphene oxide film on polystyrene foam for solar-driven interfacial water evaporation." *Journal of Materials Chemistry A* 5, no. 31 (2017): 16212-16219.
- [11] Zhou, Lin, Yingling Tan, Dengxin Ji, Bin Zhu, Pei Zhang, Jun Xu, Qiaoqiang Gan, Zongfu Yu, and Jia Zhu. "Self-assembly of highly efficient, broadband plasmonic absorbers for solar steam generation." *Science Advances* 2, no. 4 (2016): e1501227.
- [12] Yang, Yang, Ruiqi Zhao, Tengfei Zhang, Kai Zhao, Peishuang Xiao, Yanfeng Ma, Pulickel M. Ajayan, Gaoquan Shi, and Yongsheng Chen. "Graphene-based standalone solar energy converter for water desalination and purification." *ACS nano* 12, no. 1 (2018): 829-835.